Efficient experimental methods for rapid fatigue life estimation of additive manufactured elements

Efficient experimental methods for rapid fatigue life estimation of additive manufactured elements

Chiara COLOMBO[1], Andrea TRIDELLO[2], Ana Paula PAGNONCELLI[2], Carlo Alberto BIFFI[3], Jacopo FIOCCHI[3], Ausonio TUISSI[3], Laura Maria VERGANI[1], Davide Salvatore PAOLINO[2]

[1] Politecnico di Milano, Department of Mechanical Engineering, Via La Masa 1, 20156 Milan, Italy

[2] Politecnico di Torino, Department of Mechanical and Aerospace Engineering, Corso Duca degli Abruzzi 24, 10129 Turin, Italy

[3] CNR ICMATE – Institute of Condensed Matter Chemistry and Technologies for Energy, Via Previati 1/E, 23900 Lecco, Italy

* Corresponding author. E-mail: chiara.colombo@polimi.it. Tel: +390223998667.

Abstract:

Three techniques for the assessment of the fatigue response of AMed parts are compared: defect analysis and subsequent theoretical estimation of the fatigue strength with micro-CT, infrared thermography and ultrasonic fatigue testing. Experimental tests on AlSi10Mg specimens are carried out and proved that each investigated technique can be used for a rapid estimation of the fatigue response. The thermography technique and ultrasonic fatigue tests proved to be effective, evidencing the most critical defects. The fatigue response estimated starting from the defect analysis with micro-CT scans is mainly suggested for the inspection of large components.

Keywords: Additive Manufacturing; Infrared Thermography; Ultrasonic fatigue Test; Tomography; Very High Cycle Fatigue.

1. Introduction

Additive Manufacturing (AM) is emerging as an interesting technology, suitable for complex and customized shapes of components in many industrial fields, such as aerospace and automotive industries [1,2]. Selective Laser Melting (SLM) is an AM branch that reached maturity and widespread availability in the last years, exploiting the results of active research by the scientific community. Among the powders available for SLM, AlSi10Mg is one of the most studied and applied, thanks to its good weldability, low shrinkage, limited weight and reasonable mechanical properties [3,4]. The literature focused its attention on this Si-based aluminium alloy especially because of its good castability and large availability. In view of structural applications, several works focussed on the improvement of the mechanical properties of such alloys, and in particular of their fatigue performances, with thermal treatments, such as age hardening or stress relieving [5]. Indeed, increasing the fatigue resistance and understanding the damage initiation and propagation of this alloy is fundamental to properly design AM components, ensure their structural safety and speed up their time to market.

The estimation of the fatigue life for AlSi10Mg, as well as for the materials with face-centred cubic lattice, is more complex than for body-centred cubic lattice. Indeed, in the logarithmic stress vs number of cycles plots (S-N curves or Wöhler diagram), these last materials experience a horizontal asymptote, e.g. the conventional constant amplitude fatigue limit at $5 \cdot 10^6$ cycles [6]. On the other hand, aluminium alloys have a continuous decrease, with an initial slope between low and high cycle fatigue, a secondary smaller slope between High Cycle Fatigue (HCF, $10^5 < N_f < 10^7$cycles) and Very High Cycle Fatigue (VHCF, $N_f > 10^7$), and a cut-off limit at $N_f > 10^8$ [7]. In other words, the S-N curves of these materials are multi-stage fatigue life diagrams. Hence, as suggested in [8], the definition of the fatigue limit as the stress below which fatigue damage will not occur [6] or can be ignored [7] loses its meaning, and it would be more correct to substitute it by the fatigue strength at a definite number of cycles.

The presence of micro-defects typical of the SLM operating process conditions [9,10], together with the material microstructure, are responsible for the change in the S-N slope and for the fatigue performance. They play a major role when dealing with high cycle number [11]; hence, the detection and the assessment of defect criticality are crucial to estimate fatigue life.

AM is a very versatile and customizable process, but it is also prone to the generation of different defects variable in size and position, as a consequence of the laser input parameters. More in detail, it is well-known that the AM process induces two typical defects, which actively reduce the fatigue life: lack of fusion and gas porosity [12]. Their presence is

unavoidable, and they cannot be removed even with complex post-treatments, such as hot isostatic pressing [13]. It is not trivial to relate defect identification, resulting from experimental methods before or during load application, with a good and rapid prevision of fatigue life or residual fatigue life.

In this work, three techniques able to rapidly estimate the fatigue life are selected from the experimental literature: 1) the X-ray micro-computed tomography (micro-CT); 2) the Infrared (IR) thermography; 3) the ultrasonic fatigue testing. All these techniques can be extremely useful in the case of AMed parts, especially for the selection of the optimal laser parameters and of the post-additive thermal treatments. The experimental approaches and methodologies characteristic of these techniques are different. Indeed, micro-CT allows for the detection of surface or inner killer defects with a non-destructive approach that is based on the evaluation of the largest Stress Intensity Factor (SIF) [14]. On the other hand, IR thermography, applied to monitor the surface self-heating of a specimen under loading, allows determining a critical stress, corresponding to the irreversible fatigue damage initiated in the material [15]. Lastly, ultrasonic fatigue testing allows for a rapid collection of information on the fatigue behaviour of the material from the HCF to the VHCF regime [16].

The work investigates the fatigue performances of additively manufactured AlSi10Mg specimens after two different thermal treatments, aimed at controlling the spheroidization of the Si network present in the Al matrix [17,18]. These specimens are subjected to: 1) micro-CT scanning and analysis for the identification of the defects; 2) fatigue tests at increasing stress amplitude, aimed at monitoring the damage progression with IR thermography and at the estimation of the thermographic fatigue strength; 3) step-stress ultrasonic VHCF tests, aimed at estimating the full S-N curve. The focus is on the rapid assessment of the fatigue damage occurring and cumulating in this additive aluminium alloy. The aim is to find the relationship among the several types of pre-existing defects, the thermographic estimation of the fatigue strength and the corresponding number of cycles to failure. The analysis of the defect population with micro-CT inspections is currently employed for AM parts. In the paper, 16 specimens with large volumes are inspected, to verify the correlation between the largest and the critical defect and if the fatigue response can be reliably estimated starting from the micro-CT analysis. On the other hand, thermographic techniques are widely employed for the assessment of the fatigue strength of traditionally built components, but their use for AM parts is still limited. The validity of the fatigue response obtained with methodologies developed for the assessment of the fatigue strength of traditionally built components should be verified on a large number of AM datasets obtained in different conditions to be safely employed for the design of components. In this paper, different thermographic methodologies have been employed for the

assessment of the fatigue strength of AlSI10Mg specimens subjected to heat treatments with different characteristics. A novel procedure, based on ultrasonic fatigue tests carried out with a step test sequence and a statistical methodology for the analysis of data based on the accumulated damage, has been also proposed and validated experimentally. A direct comparison of the fatigue response estimated with these three methodologies, for the same batch of specimens, is more effective than comparing literature data, generally obtained with different parameters. The analysis carried out in this work can guide the choice of the most appropriate and efficient methodology for a rapid analysis of the fatigue response of AM parts.

2. Materials and Methods

2.1 Materials

AlSi10Mg samples were produced starting from spherical gas atomized AlSi10Mg powders (mean size $45\ \mu m$, dimensional range $20 - 63\ \mu m$), employing a Selective Laser Melting machine (SLM Solutions, 500 HL quad 4 × 400 W). Table 1 summarizes the powder chemical composition and the process parameters considered for the manufacturing of the specimens. All the tested specimens were manufactured with the same scanning strategy (meander), and with their main axis oriented along the building direction, i.e., the vertical direction.

Table 1: AlSi10Mg powder composition (wt. %) and SLM process parameters.

AlSi10Mg powder chemical composition							
Si	Mg	Cu	Ni	Fe	Mn	Ti	Al
10	0.4	< 0.25	< 0.05	< 0.25	< 0.1	< 0.15	bal
SLM process parameters							
Power	Plate temperature	Scanning speed	Spot size	Hatch distance	Layer thickness		
350 W	150 °C	1.15 m/s	80 µm	170 µm	50 µm		

Two thermal treatments, previously studied by the authors [17,18], were performed on the SLMed samples prior to testing:

- HT-244: annealing at 244 °C for 2 h, aimed at stress relieving samples without affecting the eutectic Si network, which characterizes as-built AlSi10Mg parts, and thus retaining an acceptable mechanical strength;

- HT-320: annealing at 320 °C for 2 h, aimed at stress relieving the produced parts and, concurrently, inducing the spheroidization of Si network. As a consequence, samples treated at this temperature exhibit lower mechanical resistance but higher ductility.

Table 2 summarizes the number of specimens used for each type of test and the name of the tested specimens within round brackets.

Table 2: Number of tested specimens.

Thermal treatment	Micro-CT	IR thermography	Ultrasonic fatigue testing
HT-244	8 (HT-244-1 ... 8)	3 (HT-244-9 ... 11)	8 (HT-244-1 … 8)
HT-320	8 (HT-320-1 … 8)	3 (HT-320-9 … 11)	8 (HT-320-1 ... 8)

The Gaussian specimen geometry [19,20] has been used for all the experimental tests. In particular, a Gaussian specimen with a risk-volume V_{90} of $2300\ \mathrm{mm}^3$ (i.e., the volume of material above the 90% of the maximum applied stress, according to [21]) has been designed. Before the tests, all the specimens have been mechanically polished with sandpapers with increasing grit (up to #1000) to remove large scratches and macro-defects. According to Table 2, micro-CT inspections have been carried out on the Gaussian specimens used for ultrasonic fatigue tests. Figure 1 shows the geometry of the tested Gaussian specimens.

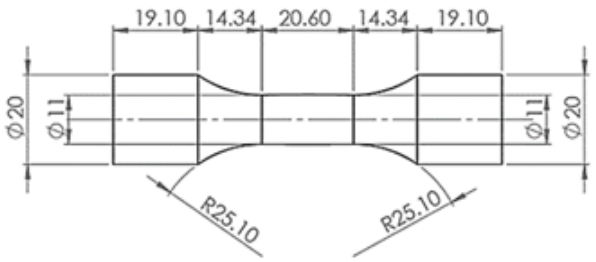

Figure 1: Geometry of the Gaussian specimen (in mm).

2.2 Methods

2.2.1 Analysis of defects with micro-CT inspections

The micro-CT is a non-destructive experimental technique that allows investigating internal defects in specimens or small components. Micro-CT inspections of all the specimens used for ultrasonic fatigue tests have been carried out by using a machine designed and built by Fraunhofer Institute, (Figure 2). This micro-CT system can reach a maximum

voltage of 300 kV and a maximum power of 30 W in the tungsten filament that generates the X-rays, the maximum distance between tube and detector is 1900 mm, while the minimum distance between tube and stage's axis of rotation is 25 mm. Using a cone-beam system, one X-ray projection in each rotating step from 0 to 360 degrees is acquired. In this work, 800 projections of each specimen were acquired with a resolution of 21.8 µm/pixel. A digital 3D image of the part, revealing the internal defects, is thereafter reconstructed from 2D images by using the software VGSTUDIO MAX 3.5, as in [14,22].

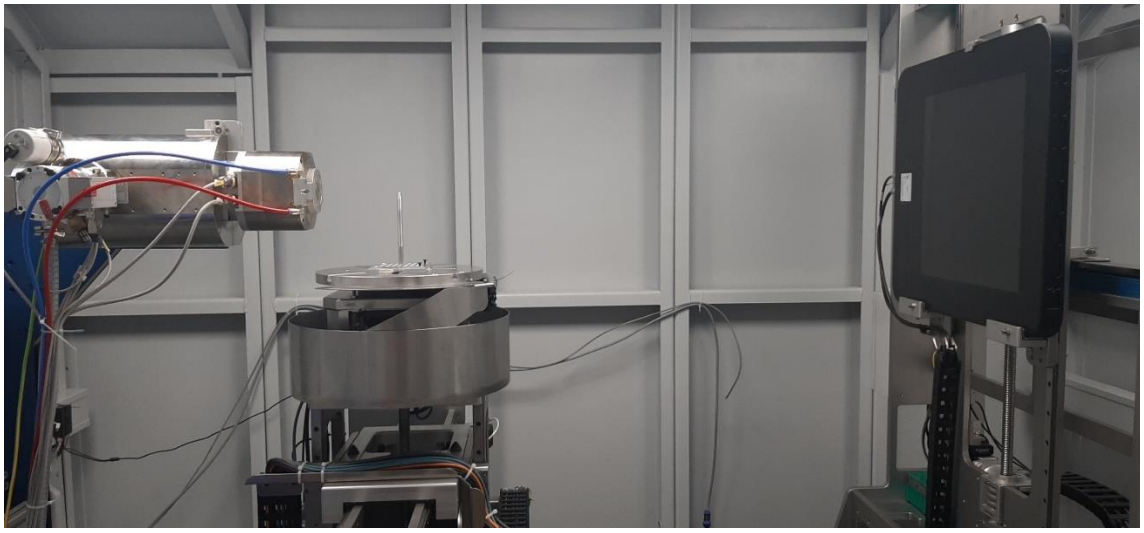

Figure 2: Details of the micro-CT equipment showing its main components: the X-ray tube, the stage that holds the specimen, and the flat detector panel.

The digital specimen is represented in the software by associating each voxel with a value on the grey scale. Darker voxels have lower grey levels and represent lower absorption of X-ray intensity, which could be caused by a void inside the material. The algorithm implemented by the Porosity/Inclusion Analysis Module, used for the identification of defects, searches for agglomerations of voxels that have low grey levels when compared to adjacent voxels. The defects size and shape are thereafter assessed by analysing the voxels present in each recognized agglomeration. Thus, the software is capable of automatically calculating information like the defect dimensions (volume, plane area, etc.), spatial position, and sphericity, which must be carefully analysed to assess the defect's influence on the fatigue response. The sphericity is provided by VGSTUDIO® as the ratio between the surface of a sphere with the same volume as the defect and the external surface of the defect:

$$Sphericity = \frac{S_{sphere}}{S_{defect}} \quad (1)$$

2.2.2 Thermographic estimation of the fatigue strength

Uniaxial fatigue tests are carried out at controlled room temperature with a servo-hydraulic testing machine (MTS Landmark) and a load cell of 100 kN capacity. The stress ratio is R=-1, constant during the whole test. Three specimens for each series are tested (HT-244-9,10,11 and HT-320-9,10,11); all these specimens are painted with a black matt (Rolma Racing TERM A.T. PAINT 100 % Silicon paint) to avoid reflection during the thermal monitoring and to increase body emissivity. Tests are performed in a room at controlled temperature; Figure 3a shows the experimental setup.

Tests consist of cyclic blocks at increasing stress amplitude, aimed at measuring the self-heating of the specimens. The initial stress amplitude of the first block, σ_1, is 40 MPa for both series. Each i-th block consists of three steps (Figure 3b):

- Step 1: ΔN=5000 cycles at the constant stress amplitude σ_i and the testing frequency f_{t1}=15 Hz;
- Step 2: 1-minute time with the specimen unloaded;
- Step 3: 2 cycles at the constant stress amplitude σ_i and the testing frequency f_{t3}=0.25 Hz.

Then, the stress semi-amplitude is increased by $\Delta\sigma$=5 MPa, and the following block starts; the test ends when the specimen fails.

All tests are thermally monitored with an IR-thermal camera endowed with InSb detectors (Model Cedip-FLIR Titanium by FLIR Systems). The camera is placed at about 30 cm from the specimen, with a resolution over the monitored area of 0.3 mm/px; the acquisition is performed at the frequency f_{at}=103 Hz. A laptop connected with the thermal camera stores, for each frame, a thermal matrix with the surface temperatures and the force signal from the load cell (reference); they are synchronised through the lock-in module. These thermal data are collected and averaged over a squared region of interest (ROI) at the centre of the specimen (25x25 px), under the hypothesis that strain fields are homogeneous at the considered spatial resolution. This means that the thermal measurements allow identifying the macroscopic fatigue damage, neglecting the thermal impact of localized defects. In other words, the aim of this thermographic approach is not to localize the critical surface defects; else, it is the rapid estimation of the fatigue performance of the bulk material.

In parallel to the thermal monitoring, also mechanical data are collected with an extensometer mounted at the centre of the specimen, e.g., storing strain measurements over the same region thermally monitored. The acquisition frequency of the extensometer is f_{ae}=25Hz.

Then, these thermal and mechanical data are processed during:

- Step 1, to obtain the thermal slope as a function of the number of cycles (*dT/dN*) from the first 4s (60 cycles), and the regime or stabilized temperature with respect to the initial temperature (ΔT_{stab}) from the last 1000 cycles [15]. Indeed, during each block, the surface temperature of the specimen increases from the room temperature up to a regime value, characteristic of each stress level. For instance, Figure 3c shows a thermogram at the stabilized temperature at the last block of a specimen. Besides, the last 1000 cycles of Step 1 are processed to obtain the dissipative signal amplitude, called *D-mode*. More in detail, the software decomposes by means of the Fourier transform the thermal signal in its harmonics with respect to the reference signal. The first harmonic is the thermoelastic signal, while high-order harmonics are taken into account with this dissipative signal [23,24]. They are related to dissipative thermal sources and inelastic local material behaviour, both for homogeneous [25,26] and composite materials [27,28].
- Step 2, to calculate the specific energy density *Q* released as heat, e.g., the dissipated heat in a unit volume per cycle, mainly related to the conduction. During fatigue cycling when the stabilization temperature is reached, if the test is suddenly stopped, e.g. at the end of Step 1, it is possible to obtain *Q* as [29,30]:

$$Q = -\frac{\partial T}{\partial t} \cdot \frac{\rho \cdot c}{f_{t1}} \tag{3}$$

where $\partial T/\partial t$ is the measured cooling rate from the first 4s after the test interruption, e.g. from the beginning of Step 2 (Figure 3d), ρ = 2700 kg·m^{-3} is the aluminium density, and c = 900 J·kg^{-1}·K^{-1} is the aluminium heat capacity;

- Step 3, to calculate two mechanical quantities from the hysteresis loop measured through the extensometer (Figure 3e). The first quantity is the mechanical energy density per loading cycle *W*, e.g., the integral of the hysteresis loop:

$$W = \oint \sigma \, d\varepsilon \tag{4}$$

This is the input work; during cycling, part of *W* generates an increase in the specimen temperature and it is related to *Q*, and part is stored into the material because of plastic deformation and damage [31]. The second quantity is the cyclic plastic strain $\Delta\varepsilon_p$, which is the width of the hysteresis loop, identifying the change in shape.

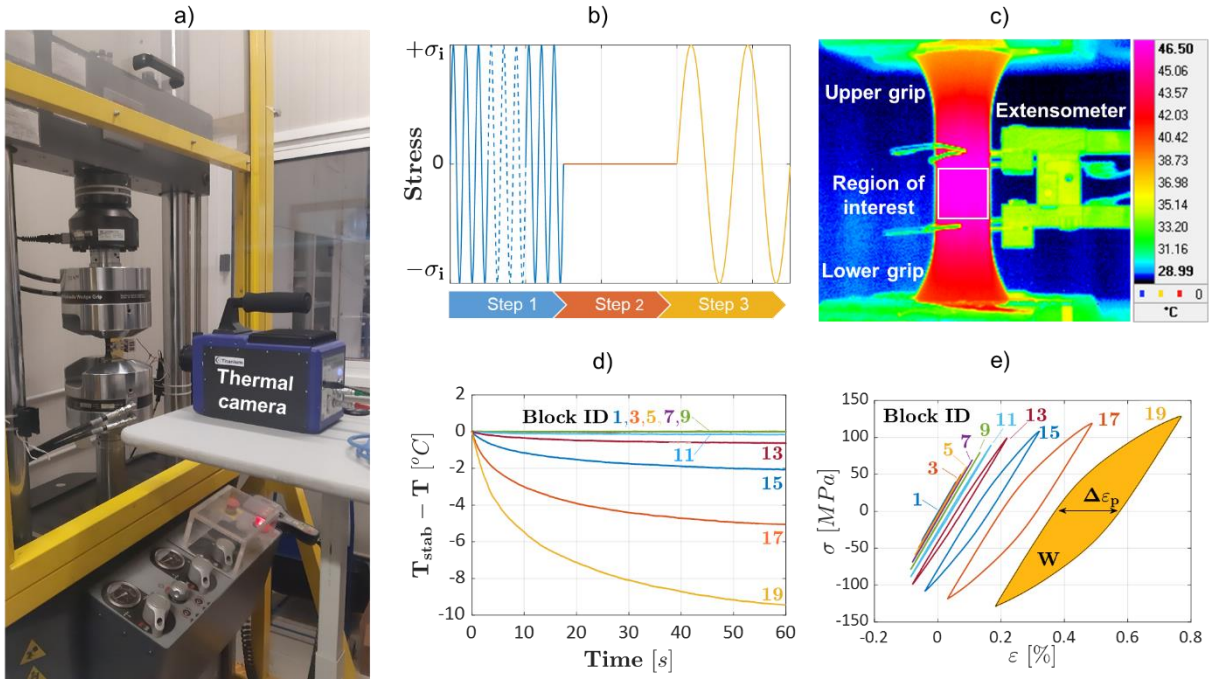

Figure 3: a) Experimental setup used for the fatigue test, thermally monitored; b) scheme of the loading block; c) thermal map of the stabilized temperature at the end of Step 1, during the last loading block; d) thermal decay during Step 2; e) stress-strain curves from Step 3, with the identification of W and $\Delta\varepsilon_p$. Data are referred to the specimen HT-320-11.

The quantities *dT/dN*, ΔT_{stab}, *Q*, *W* and $\Delta\varepsilon_p$ are calculated with the software Matlab (v.R2021a, by MathWorks); on the other hand, the *D-mod*e is estimated with the software ALTAIR LI (v.5.90.002, by FLIR Systems). All these 6 parameters experience a double behaviour with the increasing stress amplitude σ_a. To estimate the thermographic fatigue strength from each parameter, the method proposed by De Finis et al [32] is selected. As suggested in that paper, data at low stress amplitudes (the first 5 data points of each specimen) are linearly interpolated; then, the threshold value is identified as 6 times the standard deviation of the residuals. The thermographic fatigue strength corresponds to the stress of the first loading block whose residuals overcome this threshold. This procedure is automatized with a Matlab script.

2.2.3 Ultrasonic fatigue tests: experimental tests and theoretical methods

Fatigue tests have been carried out at a loading frequency of 20 kHz by using the Ultrasonic Fatigue Testing Machines (UFTMs) available at the Politecnico di Torino. Fully reversed tension-compression tests have been carried out with a step-stress scheme. The temperature at the specimen centre has been monitored in real-time with an infrared sensor. Two vortex tubes have been employed to limit the temperature increment. With this cooling system and mainly due to

the low applied stress amplitude, for all the tested specimens the measured temperature has never exceeded an upper limit value set equal to 25°C and, accordingly, the tests were carried out with no pause and ran continuously. The displacement at the specimen free-end has been continuously acquired with a laser displacement sensor. Moreover, the relation between the measured displacement amplitude and the strain at the specimen centre has been verified by measuring the strain at the specimen centre with strain gages.

In order to maximize the information contained in the experimental dataset, a step-stress test scheme has been followed. The specimen has been tested at a given stress level up to failure or up to 10^9 cycles. If the specimen has not failed, it has been tested again at a stress level increased by about 5 MPa. For each specimen, this scheme has been repeated up to failure. The results of this step-stress test have been analysed with the Cumulative Exposure Model (CEM) proposed by Nelson [33,34]. The CEM computes the damage accumulated at each loading step, according to the following assumptions:

- The number of cycles to failure at the i-th loading step is Weibull distributed with shape parameter β that does not depend on the applied stress and characteristic life η_i whose dependency on the applied stress s_i is modelled with the Basquin's law:

$$F_i(n) = 1 - e^{-\left(\frac{n}{\eta_i}\right)^{\beta}} = 1 - e^{-\left(\frac{n}{s_i^{-p}/k}\right)^{\beta}} = 1 - e^{-(k \cdot n \cdot s_i^{p})^{\beta}}, \quad (5)$$

  where $F_i(n)$ denotes the Weibull cumulative distribution function (cdf) at the i-th loading step, and k and p are the parameters of the Basquin's law. The cumulative distribution function (cdf) quantifies the probability of having a random sample below a specific value, $F_X(x) = P[X \leq x]$, where $F_X(x)$ denotes the cdf of the random variable X evaluated at x and $P[X \leq x]$ is the probability of having a random variable X smaller than x. From a practical point of view, let us consider X as the random number of cycles to failure and x a specific number of cycles to failure (e.g., 10^6 cycles), then $F_X(x)$ quantifies the probability that, in a test, the number of cycles to failure is below x (e.g., 10^6 cycles).

- At the beginning of the $(i+1)$-th loading step, the corresponding cdf starts at the failure probability accumulated up to the i-th loading step:

$$F_{i+1}(n_{eq,i}) = F_i(n_i + n_{eq,i-1}), \quad (6)$$

  where $n_{eq,i}$ is the initial equivalent life for the $(i+1)$-th loading step, $n_{eq,i-1}$ is the initial equivalent life for the i-th loading step and n_i is the number of cycles run at i-th loading step.

Figure 4 depicts the application of the CEM for a step-stress test consisting of three loading steps. Each loading step is run at applied stress equal to s_i for n_i cycles, being $i = 1,2,3$ and $s_1 < s_2 < s_3$.

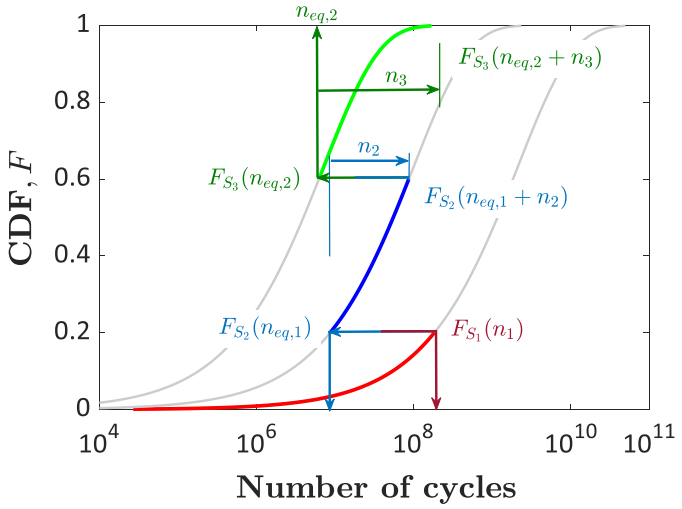

Figure 4: Scheme of application of the Cumulative Exposure Model for a step-stress consisting of three loading steps.

The i-th initial equivalent fatigue life can be easily obtained from Eqs. (5) and (6), by considering $n_{eq,0} = 0$:

$$n_{eq,i} = \sum_{j=1}^{i} n_j \left(\frac{s_j}{s_{i+1}}\right)^p. \tag{7}$$

From the expression of the initial equivalent fatigue lives in Eq. (7) and by applying the assumptions of the CEM in Eqs. (5) and (6), it is possible to define the cdf of the fatigue life in a step-stress test run up to failure:

$$F_{CEM}(n_f) = 1 - e^{-\left(k\left(\left(n_f - \sum_{j=1}^{i-1} n_j\right)s_i^p + \sum_{j=1}^{i-1} n_j s_j^p\right)\right)^\beta} = 1 - e^{-\left(k s_i^p n_{f,eq}\right)^\beta}, \tag{8}$$

where it has been assumed that failure occurs at the generic i-th loading step, at a total number of cycles equal to n_f, and $n_{f,eq}$ is the equivalent fatigue life up to failure:

$$n_{f,eq} = \left(n_f - \sum_{j=1}^{i-1} n_j\right) + \sum_{j=1}^{i-1} n_j \left(\frac{s_j}{s_i}\right)^p. \tag{9}$$

It is worth noting that the CEM in Eq. (8) is a probabilistic application of the Miner's rule. This can be demonstrated by substituting in Eq. (8): i) ks_j^p with $1/N_j$ for $j = 1, \dots, i$; ii) n_j with Δn_j for $j = 1, \dots, i-1$; iii) $\left(n - \sum_{j=1}^{i-1} n_j\right)$ with Δn_i. The proposed substitutions yield a final cdf equal to:

$$F_{CEM}(n_f) = F_{Miner}(d_{tot}) = 1 - e^{-\left(\frac{d_{tot}}{1}\right)^\beta}, \tag{10}$$

where $d_{tot} = \sum_{j=1}^{i} \frac{\Delta n_j}{N_j}$ is the total damage accumulated up to failure, according to the Miner's rule. As reported in Eq. (10), the CEM implicitly considers the total damage as Weibull distributed with shape parameter equal to β and characteristic life equal to one. Therefore, according to the CEM, the Miner's damage up to failure is below one in the 63.2% of cases, whereas it can be larger than one in the remaining 36.7% of cases.

The application of the CEM first requires fitting of the three parameters (i.e., k, p, and β) involved in Eq. (8). Parameter fitting is obtained by minimizing the sum of squared errors between the empirical and the theoretical cdfs. The empirical cdf is computed according to the Benard's approximation for median ranks [35] by sorting in ascending order the equivalent fatigue lives up to failure $n_{f,eq}$ in Eq. (9). Since the quantity $n_{f,eq}$ depends on the unknown parameter p, the fitting process is iterative and consists of the following steps:

1. Assume a first guess for parameter p, p^*.
2. For the m-th specimen, compute $n^*_{f,eq,m}$ according to Eq. (9). If n_{sp} is the total number of tested specimens, then n_{sp} values of $n^*_{f,eq}$ must be computed.
3. Sort the n_{sp} values of $n^*_{f,eq}$ in ascending order.
4. Compute the empirical cdf for the $\underline{m}$-th sorted $n^*_{f,eq}$, according to the Benard's approximation for median ranks:

$$F^*_{exp,\underline{m}} = \frac{\underline{m}-0.3}{n_{sp}+0.4}. \tag{11}$$

   Then n_{sp} values of F^*_{exp} must be computed.
5. From the n_{sp} values of F^*_{exp} in Eq. (11) and from the sorted $n^*_{f,eq}$, estimate parameters k^* and β^*, with the least squares method, according to the linearized model obtained from Eq. (8):

$$\log\left(-\log\left(1-F^*_{exp,\underline{m}}\right)\right) = \beta^*\left(\log(k^*) + \log\left(s^{p^*}_{f,\underline{m}}\right)\right) + \beta^*\log\left(n^*_{f,eq,\underline{m}}\right) + \varepsilon_{\underline{m}}, \tag{12}$$

   where $\underline{m} = 1, \dots, n_{sp}$, $s_{f,\underline{m}}$ is the stress applied when the $\underline{m}$-th specimen has failed, and $\varepsilon_{\underline{m}}$ is the error term between the theoretical and the empirical cdfs for the $\underline{m}$-th specimen. The estimated parameters minimize the sum of squared errors for the assumed guess for parameter p.
6. Compute the sum of squared errors SSE^*, corresponding to the set of parameters (p^*, k^*, β^*).
7. If SSE^* is minimum, then the final set of parameter estimates is equal to (p^*, k^*, β^*). Otherwise, assume a new p^* value and repeat steps from 1 to 7.

The iterative process has been implemented in Matlab® and the minimization algorithm is based on golden section search and parabolic interpolation.

3. Experimental results

3.1 Manufacturing defects: micro-CT inspection

Figure 5a shows the micro-CT scan of the HT-244-1 specimen over the inspected volume, roughly corresponding to the specimen risk-volume, i.e., the critical region where the fatigue crack is more likely to originate from defects. The whole defect population is shown in Figure 5a. Figure 5b shows a frontal slice of the inspected volume. The defects are identified and ordered by considering their area in the x-y plane ($a_{0,CT}$), corresponding to the plane perpendicular to the direction of the maximum applied load. The red cross indicates the defect with the largest $a_{0,CT}$. Figure 5c and Figure 5d show the cross-section slice where the largest defect identified in Figure 5b lays, being Figure 5c the slice without the defect analysis, i.e. in grayscale, and Figure 5d the same slice with the identified defects coloured according to the size colormap.

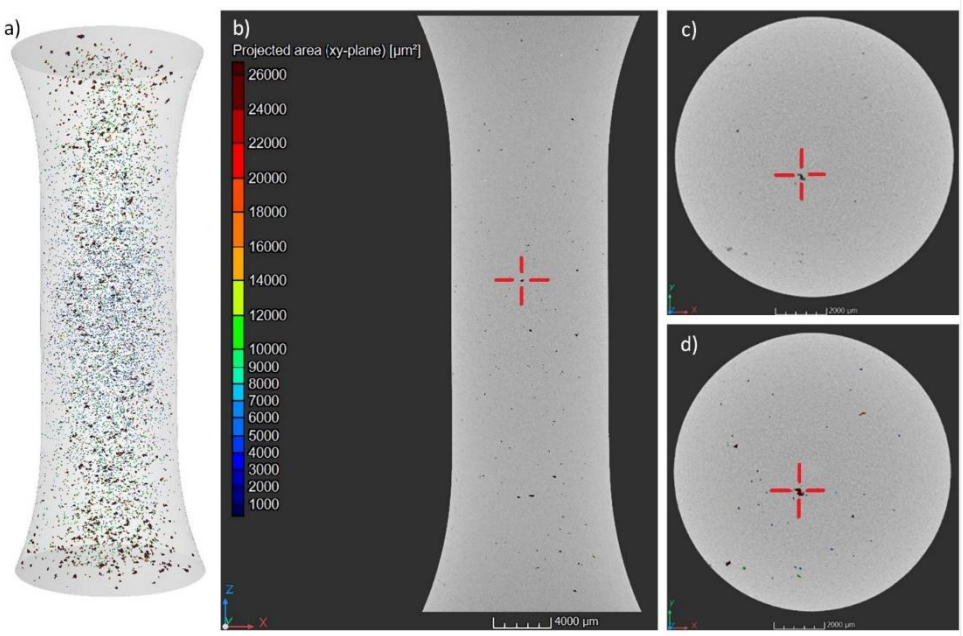

Figure 5: Representative image showing the results of the micro-CT-scan of the specimen HT-244-1: (a) inspected volume and whole defect population; (b) Frontal slice showing the defect with the largest area in a plane perpendicular to the axial direction. (c) Cross-section slice containing the same defect before the defect analysis and (d) after the analysis.

Figure 6 plots the sphericity of all the investigated defects with respect to the square root of $a_{0,CT}$ for the HT-244 specimens (Figure 6a) and for HT-320 specimens Figure 6b). According to these plots and in agreement with literature results [12,36], the sphericity tends to reduce with the defect size. Therefore, the shape of the defects becomes more irregular as $\sqrt{a_{0,CT}}$ increases. This trend has been found for both heat treated series. The heat treatment, moreover, does not seem to affect the defect size [5]. The data show the same trend, with the largest defect smaller than 400 µm in both cases. This trend fits well with the typical defects population generated by AM: small and round pores and large but also irregular shape defects, namely lack of fusion, that can be locally generated by an excess of energy given to the powder layer and under an insufficient energetical condition, respectively [9]. Typically, the co-presence of both these defects can be detected near the optimal process condition.

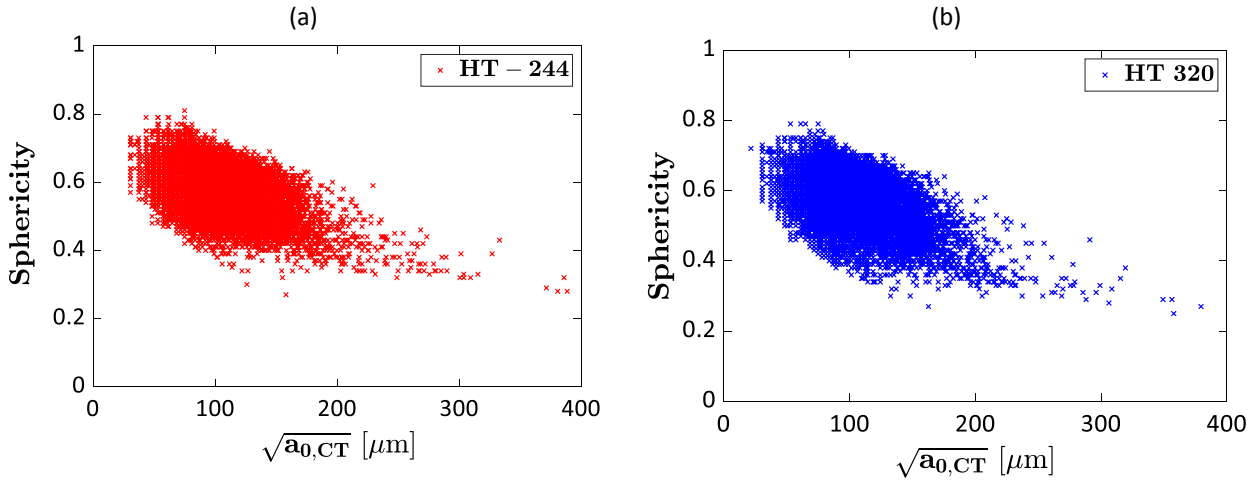

Figure 6: Defect sphericity with respect to the area of the defect in a plane perpendicular to the maximum applied stress: a) HT 244; b) HT 320.

The analysis has been thereafter focused on the largest defect. Indeed, according to [21], the largest defect is the one that controls the fatigue response and that must be considered for the design of components. The square root of the area of the largest defect for each tested specimen, $\sqrt{a_{0l,CT}}$, has been considered in the following analysis and assumed to follow a Largest Extreme Value Distribution (LEVD) [37]. Figure 7 plots the $\sqrt{a_{0l,CT}}$ and the estimated LEVD models on a Gumbel plot for the HT-244 and the HT-320 specimens.

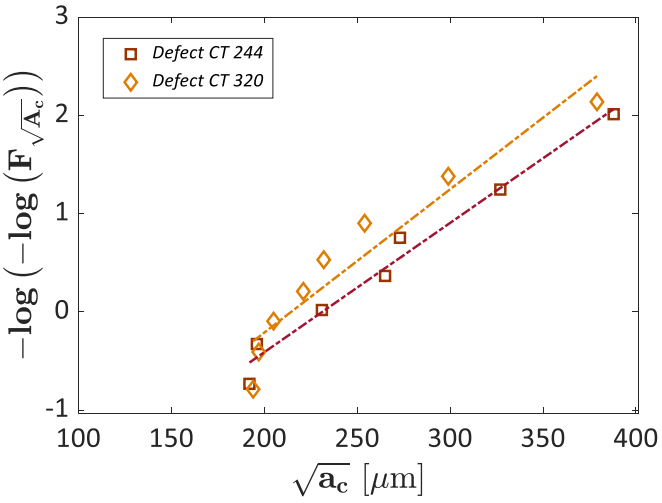

Figure 7: Gumbel plot of the largest defect in each tested specimen measured with micro-CT inspections.

According to Figure 7, the LEVD properly fits the experimental data. The defects in the HT-244 specimens are larger than the defects in the HT-320 specimens. However, the difference is limited, with the largest defect in the HT-320 being about 2% smaller than the largest defect in HT-244 specimens. The information on the largest defect in each specimen can be exploited for assessing the allowable stress to be considered for the design of components. For example, the limit stress can be computed with the widely used "El Haddad" model [38,39], which provides the limit stress for short cracks as a function of the SIF threshold for long cracks, $K_{th,LC}$, and of the fatigue limit for a defect-free material, $s_{l,fd}$. In particular, the "El Haddad" formulation models the dependence between the fatigue strength and the defect size, with a smoother transition between the short crack to the long crack regime. The limit stress can be obtained from $s_{l,fd}$, the defect size, $\sqrt{a_{0l,CT}}$, and by considering the El-Haddad-Smith-Tropper material length parameter defined as:

$$\sqrt{a_0} = \frac{1}{\pi} \cdot \left(\frac{\Delta K_{th,LC}}{Y \cdot \Delta s_{l,fd}}\right)^2 \tag{13}$$

where Y is a shape factor accounting for the defect location, (i.e., $Y = 0.65$ for surface defects). For a proper application of this formulation, the $\Delta \mathrm{K_{th,LC}}$ and the $\Delta \mathrm{s_{l,fd}}$ values should be experimentally estimated, but this would require time-consuming and expensive experimental tests. Accordingly, they have been reliably estimated with literature available models. The fatigue limit has been estimated as $s_{l,fd} = 1.6 \cdot HV$ (equal to 113.7 ± 2.0 HV and to 74.7 ± 2.6 HV for the HT-244 and HT-320 specimens, respectively), according to [38], whereas $\mathrm{K_{th,LC}}$ should be in the range $[1\text{:}\,3]$ $\mathrm{MPa}\sqrt{\mathrm{m}}$, according to [40], and has been assumed equal to 3 $\mathrm{MPa}\sqrt{\mathrm{m}}$. The limit stresses computed by considering the smallest and the largest defect found through micro-CT analyses are equal to 107 and 125 MPa, for the HT-244 specimens, whereas they are equal to 89 MPa and 101 MPa for the HT-320 specimens. It must be noted, however, that the

estimated limit stresses are affected by the uncertainty in the assumption of the $s_{l,fd}$ and $K_{th,LC}$, even if reasonable values have been assumed by considering widely adopted literature models. This analysis showed that a fatigue limit stress can be reliably computed starting from the defect population assessed with micro-CT inspections but, for more accurate results, experimental tests to assess the $s_{l,fd}$ and $K_{th,LC}$ are required and suggested.

According to [41], the specimen microstructure, accounted by the Vickers hardness [21] , significantly affects the fatigue response, together with the defect size. The Vickers hardness of HT-320 is smaller than that of HT-244 (113.7 HV ± 2.0 for the HT-244 specimens and 74.7 HV ± 2.6 for the HT-320 specimens). Accordingly, the significant weakening of the microstructure induced by the HT-320 has a strong effect and counterbalances the presence of larger defects in HT-244 specimens, which thus show a larger limit stress.

It must be noted that the limit stresses have been computed by considering the largest defect and its actual area provided in output by the software VG studio, according to a procedure commonly followed with micro-CT inspections. Since the largest defects are those characterized by the smallest sphericity, it can be concluded that the critical defects are those characterized by low sphericity. However, to account for the influence of the sphericity and the irregular shape of defects, an equivalent or effective defect size (following the indications provided in [21]) has been considered for the critical defects observed on the fracture surfaces, as discussed in Section 3.3. and 4.

3.2 Thermographic analysis

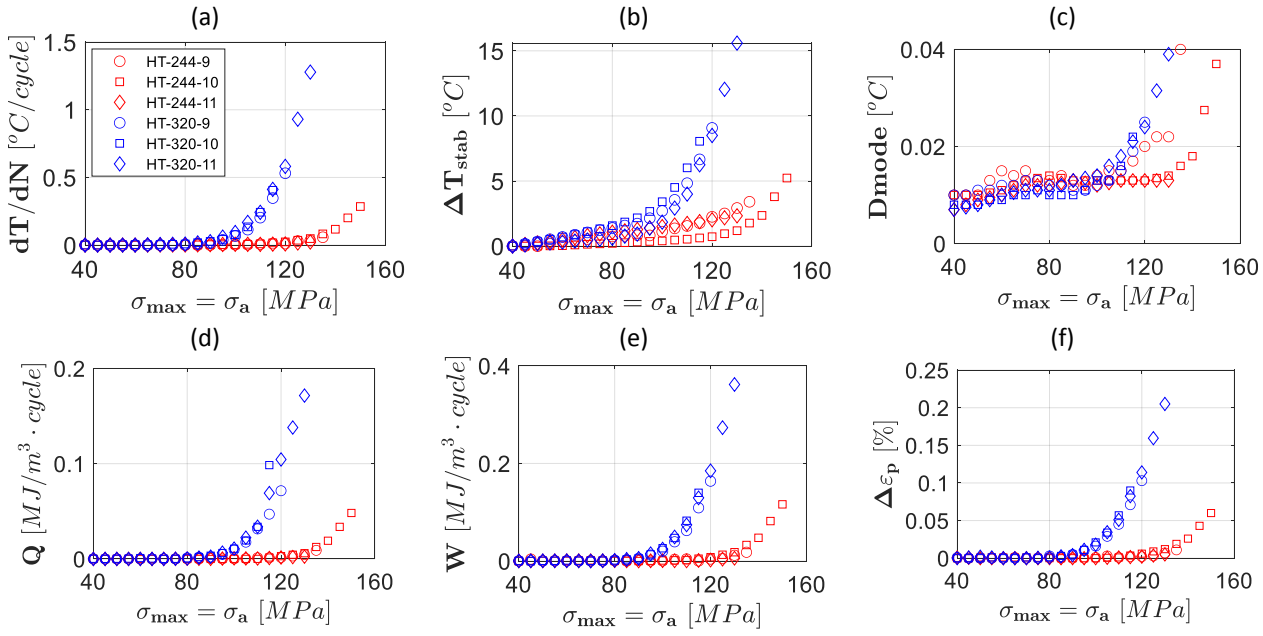

Figure 8: Thermal and mechanical quantities as a function of the applied stress: a) thermal slope as a function of the number of cycles, dT/dN (from Step 1); b) stabilized temperature, ΔT_{stab} (from Step 1); c) dissipative signal amplitude,

D-mode (from Step 1); d) dissipated heat, Q (from Step 2); e) mechanical work, W (from Step 3); f) cyclic plastic strain, $\Delta\varepsilon_p$ (from Step 3).

Figure 8 plots the thermal and mechanical quantities as a function of the applied stress amplitude σ_a, equal to the maximum stress σ_{max}. In particular, *dT/dN*, ΔT_{stab} and the *D-mode* are the thermographic quantities obtained from Step 1, *Q* is the thermographic quantity obtained from Step 2, and W and $\Delta\varepsilon_p$ are the mechanical quantities obtained from Step 3. The thermographic fatigue strength is estimated from each plot with the threshold method of [32] as previously mentioned in Sect. 2.2.2, and Table 3 gives the resulting values for each specimen.

Figure 9 summarized these results. Here, the stress data of Table 3 are grouped based on the different thermographic quantities, averaging the stress values from the 3 specimens of each thermal treatment, e.g., 3 averaged values for each bar. Besides, the last two bars of Figure 9 are obtained calculating the average from all the thermographic quantities and specimens, e.g., 18 averaged values.

Table 3: Estimations of the thermographic fatigue strength, obtained with the threshold method suggested in [32].

	Thermographic fatigue strength [MPa] from each quantity					
Specimen ID	***dT/dN***	***ΔT_{stab}***	***D-mode***	***Q***	***W***	***$\Delta\varepsilon_p$***
HT-244-9	95	120	120	100	105	130
HT-244-10	120	120	140	120	120	120
HT-244-11	130	120	130	100	130	100
HT-320-9	95	95	100	95	80	80
HT-320-10	85	70	110	90	90	90
HT-320-11	90	90	100	90	90	100

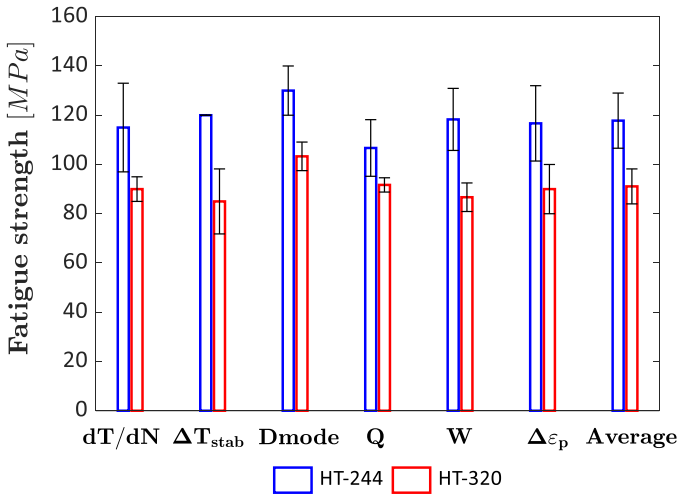

Figure 9: Thermographic fatigue strength, with the average and standard deviation values, estimated from the different quantities and for each thermal treatment.

3.3 Ultrasonic fatigue test results

For each heat-treatment condition, eight ultrasonic fatigue tests have been run. The first HT-244 specimen has prematurely failed in the first step-loading and, for this reason, it has been discarded from the analysis of the test results. Table 4 reports the fatigue data for the step-stress tests run on HT-244 and HT-320 specimens.

The raw data reported in Table 4 can be also depicted in an S-N plot, as shown in Figure 10. The different colours used in Figure 10 differentiate the tested specimens. Runout data are denoted with triangles, whereas failures with cross symbols. Specimens that failed at the first loading step are marked with a single cross symbol (244-5, 244-7, 244-8 in Figure 10a and 320-6, 320-7 and 320-8 in Figure 10b). Specimens that were retested after a runout, on the other hand, are those plotted with triangle marks (at the runout stress amplitudes) and a cross symbol (at the failure stress amplitude).

Table 4: Step-stress tests run on HT-244 and HT-320 specimens.

Specimen name	Number of cycles	Applied stress [MPa]
244-2	[1.00E+09; 3.38E+06]	[55; 60]
244-3	[1.00E+09; 1.00E+09; 8.28E+08]	[49; 55; 60]
244-4	[1.00E+09; 1.28E+08]	[51; 56]
244-5	1.06E+08	60
244-6	[1.00E+09; 1.67E+08]	[66; 71]
244-7	8.70E+06	77
244-8	7.89E+06	75
320-1	[1.00E+09; 1.00E+09; 1.00E+09; 1.00E+09; 1.00E+09; 1.00E+09; 1.06E+06]	[36; 41; 45; 50;54; 59; 63]
320-2	[1.00E+09; 2.90E+07]	[45; 50]
320-3	[1.00E+09; 1.00E+09; 1.00E+09; 1.00E+09; 1.00E+09; 4.08E+06]	[41; 45; 50; 54;59; 63]
320-4	[1.00E+09; 1.00E+09; 1.00E+09; 1.00E+09; 6.73E+08]	[52; 56; 61; 66;70]
320-5	[1.00E+09; 1.00E+09; 9.64E+07]	[63; 68; 72]
320-6	8.17E+06	72
320-7	4.18E+07	75
320-8	7.83E+06	80

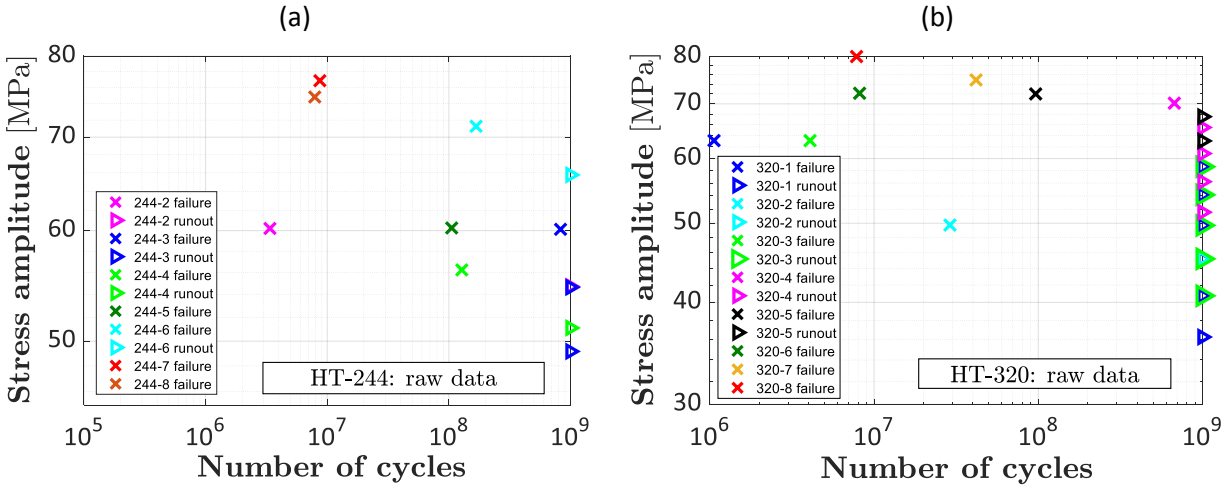

Figure 10: Results of step-stress tests in S-N plots: a) HT-244 specimens; b) HT-320 specimens.

Figure 11a depicts in a P-P plot the good agreement between empirical and theoretical cdfs, after the completion of the fitting process for both heat-treated specimens (HT-320 specimens in blue and HT-244 specimens in red). The high correlation between the two cdfs is confirmed by coefficients of determination larger than 93%.

Once parameter p has been estimated, it is then possible to compute an equivalent fatigue life up to failure for each specimen, according to Eq. (9). An equivalent S-N diagram of the dataset can be plotted from the set of equivalent fatigue lives up to failure (Eq. (9)): each datapoint, which corresponds to a specific specimen, has x-coordinate equal to $n_{f,eq}$ (i.e., the equivalent fatigue life up to failure for the considered specimen) and y-coordinate equal to s_f (i.e., the applied stress when the considered specimen has failed in the step-stress test). Figure 11b shows the equivalent S-N diagram for both heat-treated specimens.

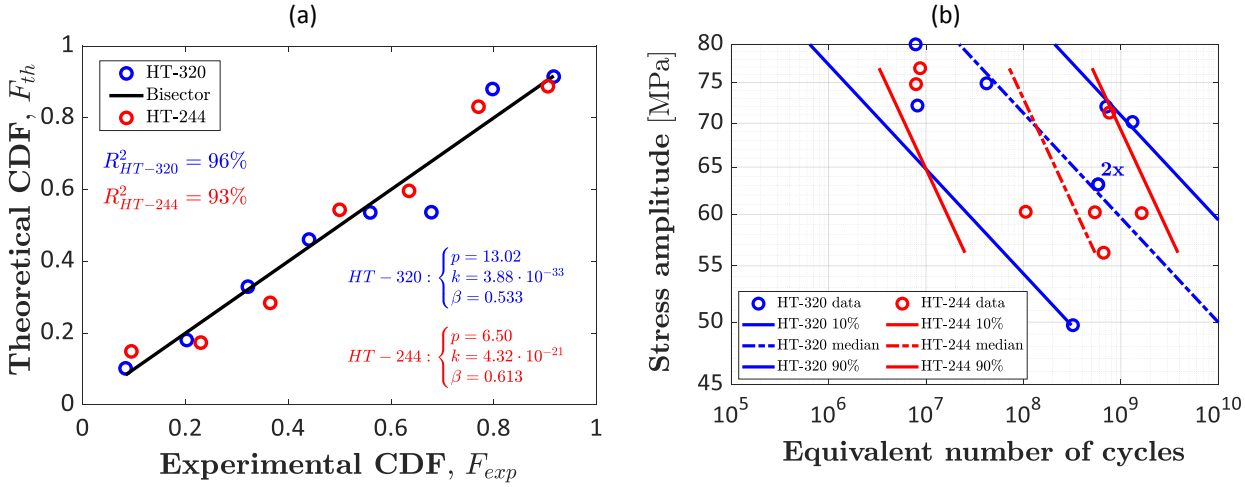

Figure 11: Fitting results of step-stress tests: a) P-P plot for HT-320 and HT-244 specimens at the end of the fitting process b) Equivalent S-N diagram for the tested specimens.

The Probabilistic-S-N (P-S-N) curves that are depicted in Figure 11b have been estimated by considering, in the following expression, values of the failure probability α equal to 10%, 50% (median curve) and 90%:

$$\log(n_{f,eq}) = -p\log(s_f) + \frac{\log(-\log(1-\alpha))}{\beta} - \log(k), \tag{14}$$

where the parameters k, p, and β have been substituted by their estimates.

3.3.1 Fracture surface analysis

Fracture surfaces have been also observed with the Scanning Electron Microscope (SEM) to investigate the crack origin. All the fatigue failures originated from a manufacturing defect: in the following, the defect at the origin of the fatigue failure will be called "critical defect". Surface defects were found to be the most critical defects regardless of the heat treatment, with all the fatigue failures concentrated in a region close to the surface and with a maximum distance of 0.250 mm. Pores and cluster of pores, irregular surface defects, lack of fusion defects or cluster of defects were at the origin of all the failures, with no influence of the heat treatment. Figure 12 shows representative defects found at the origin of the fatigue failures: Figure 12a shows a sub-surface pore, Figure 12b shows a lack of fusion defect and Figure 12c shows a cluster of pores and incomplete fusion defect.

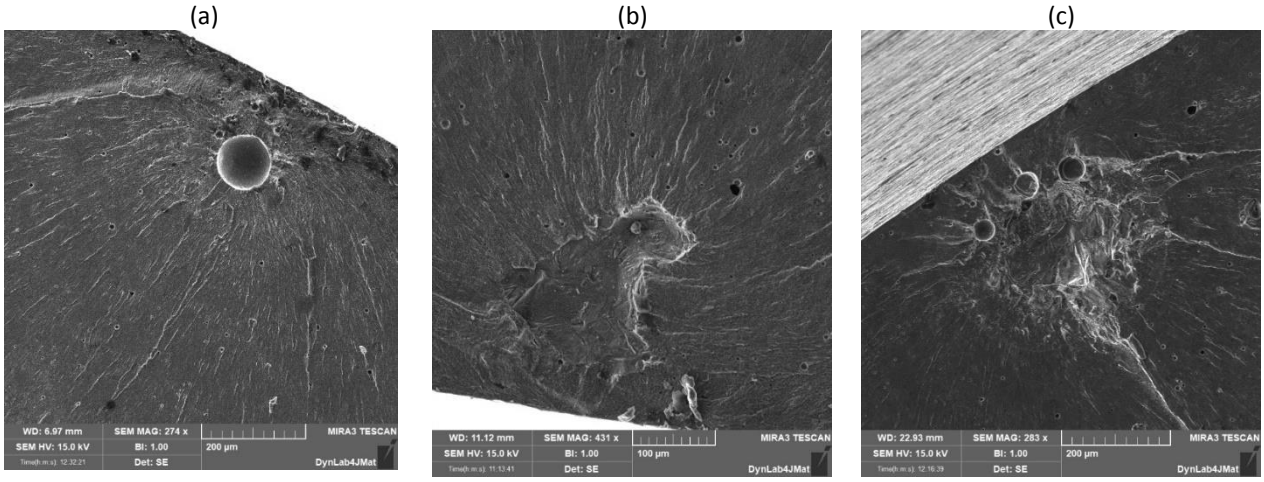

Figure 12: Representative defects found at the origin of the fatigue failures: a) large pore close to the surface (HT-320-5); b) incomplete fusion defect (HT-320-8); c) cluster of pores and incomplete fusion defect (HT-244-4).

According to [21], the square root of the area of the critical defect projected on a plane perpendicular to the maximum applied stress, $\sqrt{a_c}$, is assumed to follow a LEVD (with cdf $F_{\sqrt{A_c}}$) as for the largest defects assessed with micro-CT scans. For defects with irregular morphology, with different origins and clusters of defects, an equivalent defect area has been estimated, according to the rules provided in [21]. With this procedure, defects characterized by different morphology

and irregular shapes can be compared, since their actual influence on the fatigue response from a fracture mechanics point of view is considered. Similarly, the approach in [37] allows also to discriminate if a defect close to the surface behaves like a surface or an internal defect. Indeed, the defect location significantly affects the fatigue response, with surface defects or defects in touch with the surface being more detrimental for the fatigue response, since characterized by larger SIFs.

Figure 13a shows, in a Gumbel plot, the $\sqrt{a_c}$ distribution estimated by considering the equivalent size. For the sake of comparison, the cdfs estimated by considering the $\sqrt{a_{0l,CT}}$ are also shown (grey line for the HT-244 and black line for the HT-320). In Figure 13b, the $\sqrt{a_c}$ estimated by considering the actual defect size and the $\sqrt{a_{0l,CT}}$ (i.e., square root of the area of the largest defects assessed through micro-CT inspections) are also compared.

According to Figure 13a, the critical defects in HT-244 specimens are larger than those in HT-320 specimens. However, the difference between the critical defects in HT-244 and in HT-320 is larger than that found by considering the micro-CT largest defects. Indeed, the largest defect found through micro-CT analyses did not correspond to the critical defect for all the investigated specimens. For example, the largest defect found on the fracture surfaces of HT-320 specimens is about 32% smaller than the largest critical defect in HT-244 (this percentage difference reduced to 3% by considering the $\sqrt{a_{0l,CT}}$). This discrepancy can be explained by considering that $\sqrt{a_{0l,CT}}$ are computed as the actual area of the defects (i.e., the area included within the outer boundary of the defect), whereas $\sqrt{a_c}$ is the equivalent defect size. This can be verified by analysing Figure 13b, in which $\sqrt{a_c}$ is computed by considering the real area of the defect. As shown in Figure 13b, the difference between the actual $\sqrt{a_c}$ measured on fracture surfaces of HT-244 and HT-320 is significantly reduced, being close to that estimated by considering the CT defects.

The reason why defects after the HT-244 heat treatment are larger must be also investigated. Indeed, according to [42,43], low-temperature heat treatments should not affect the defect population and the defect size. By considering all the defects found in the investigated specimens with micro-CT inspections (Figure 6 and Figure 7), no evident differences between the population of defects in the two investigated heat-treated conditions have been found. Moreover, all critical defects were found to be close to the surface and with similar origin and typology (mainly pores, lack of fusion defects), regardless of the heat treatment. An influence of the heat treatment on the defect type and locations can be also excluded. Therefore, it can be inferred that the different characteristic sizes of the defects after the two heat treatments can be mainly ascribed to the randomness of the defect size and to the quite limited number

of tested specimens. According to [44], even if the same process parameters are considered for manufacturing the specimens, significant differences in the defect population and size can be found. Many "hidden" factors can affect the random occurrence of a defect, like the location of the specimen on the building platform. To support this explanation, it must be considered that the $\sqrt{a_{0l,CT}}$ in Figure 7 do not show a significant difference, with the estimated cdfs following the same trend. By increasing the number of available data, the difference would be probably reduced also for critical defects found on the fracture surfaces. Further proofs for this explanation can be found in Figure 13c, which plots all the defects together, without discriminating between heat treatments. The largest CT defects and the critical defects are plotted, together with the estimated LEVD. In Figure 13c, the legend *FS defects* refers to fracture surface defects, whereas the legend *CT defects* refers to defect sizes assessed with micro-CT scans.

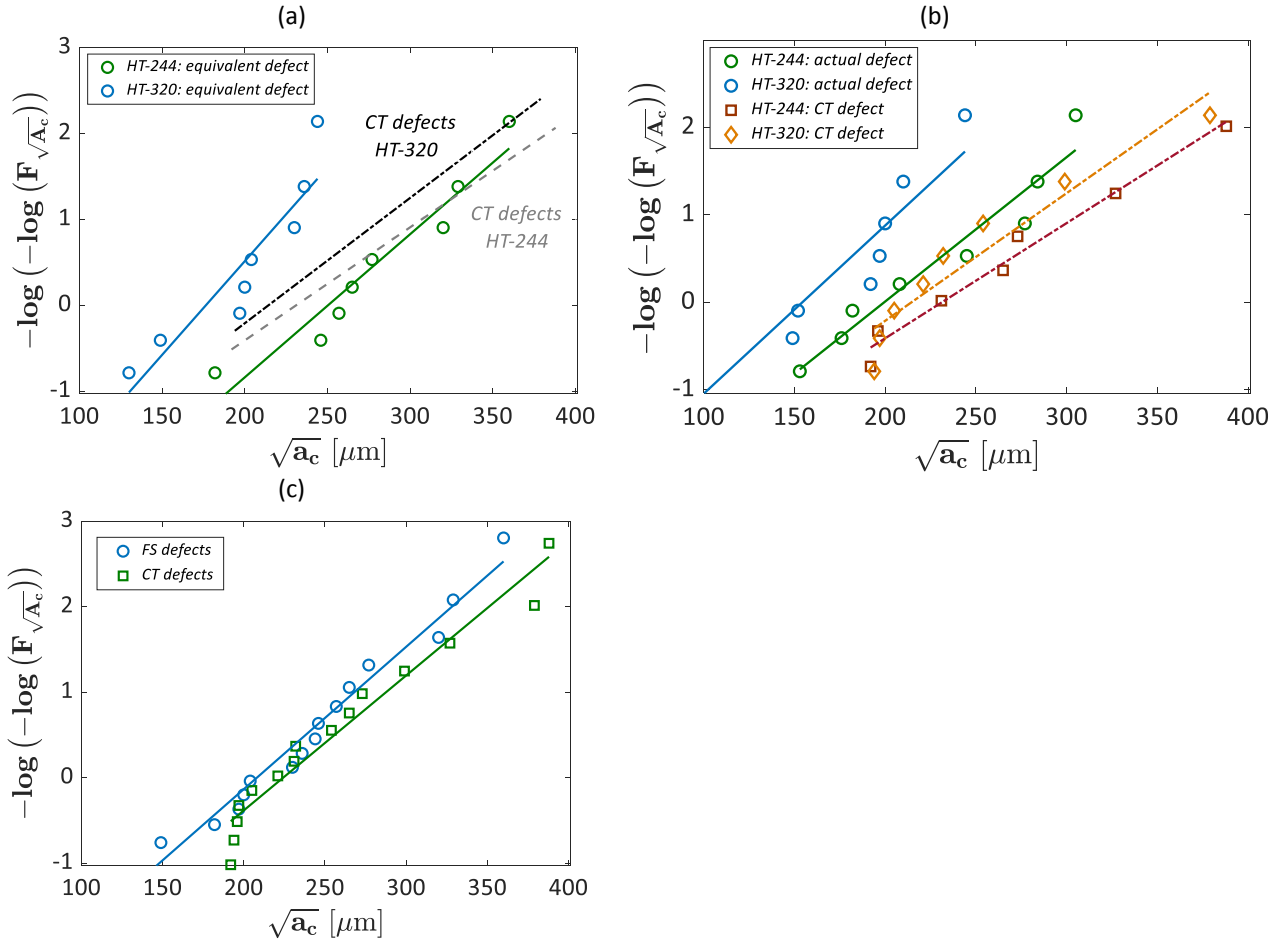

Figure 13: Gumbel plot of the most critical defects in the investigated specimens: a) equivalent size of the critical defect originating the fatigue failures observed on the fracture surfaces; b) square root of the real area of the critical defects measured on the fracture surfaces and square root of the area of the largest defects assessed through micro-CT inspection; c) defect size assessed through micro-CT inspections and observed on the fracture surfaces, without distinguishing between the heat treatments.

As shown in Figure 13c, the LEVD well fits all the FS and the CT defect characteristic sizes, and a unique trend is found. The estimated LEVDs follow the same trend, with limited differences. This analysis confirms that, with the available data, the differences of $\sqrt{a_c}$ after the two heat-treatments can be ascribed to the large scatter of the defect size within the investigated volume and to the random location of defects within the cross-section, with HT-244 defects mainly characterized by larger equivalent sizes, even with similar actual areas.

4. Discussion

This Section analyses and discusses the strength and weaknesses of the three investigated methodologies for the assessment of the fatigue strength of AM components.

Micro-CT analyses provide a large amount of information on the defect population within the manufactured component. This information can be exploited to assess the fatigue strength to be considered when the components are designed. Information on the sphericity, the morphology and the defect location can be obtained only through micro-CT analyses and not with the other investigated techniques. However, the micro-CT scan fails to provide an indication of the defect criticality. Indeed, the analysis of the fracture surfaces has confirmed that, for all the investigated specimens, the largest defect is not the most critical. Two are the main reasons for this result. The first one is related to the stress distribution within the loaded volume, which is almost uniform in Gaussian specimens, but it anyway varies within a 10% range, according to the V_{90} definition [21]. The second one, on the other hand, is related to the defect location. Indeed, defects close to the surfaces are more critical than internal defects. Accordingly, larger internal defects can be less critical, since characterized by a smaller SIF.

In this analysis, an influence of the residual stresses on the crack origin distribution can be excluded. The two investigated heat treatments provide small values of residual stresses at the surface [18,45] and, according to [46–49], a similar trend is reasonably expected in the sub-surface region. All the critical defects have been found in a small region close to the surface, thus subjected to similar values of residual stresses, regardless of the heat treatment. Accordingly, the stress distribution and the equivalent defect size have a prevalent influence with respect to the residual stresses. This analysis highlights that the estimation of the limit stress starting from the defect population assessed with micro-CT analysis cannot take into account the influence of residual stresses or local material properties variation. For example, if residual stresses are high in a material region and influence the fatigue response, the fatigue crack will start

in this region, regardless of the defect size. On the other hand, the fatigue strength computed by considering the largest defect assessed with micro-CT inspections will not change depending on the local material properties.

Figure 14 compares, for each tested HT-244 and the HT-320 specimens, the SIFs computed by considering the critical defect and the largest defect. The SIF values in the loaded volume are computed by considering the local stress amplitude at the defect location. The local stress amplitude is computed by measuring the exact defect location within the specimen, with image processing of the fracture surfaces images for the radial direction and by using a high-resolution digital calliper for the longitudinal direction. A Finite Element model of the Gaussian specimen has been created with the commercial software Ansys by using plane elements, due to specimen axisymmetry. A modal analysis has thereafter been carried out to compute the ratio between the stress amplitude at the specimen centre and the local stress at the defect location. With this procedure, the local stress involved in the crack nucleation process has been computed.

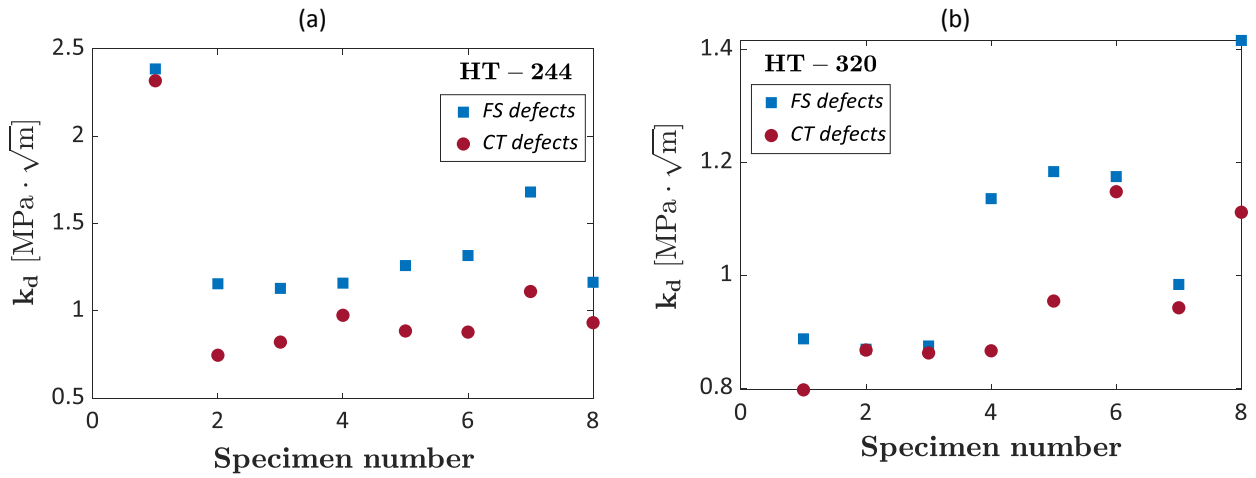

Figure 14: Comparison of the SIF computed by considering the critical defect on the FS and the largest micro-CT defect: a) HT-244 specimens; b) HT-320 specimens.

According to Figure 14, the SIF computed for CT defects is smaller than the SIF computed for the FS defects. This analysis justifies why the crack does not originate from the largest defect within the loaded volume, in agreement with literature results [50,51]. Therefore, although micro-CT inspections have proved to be effective in assessing the defect population, they may fail to provide indications on the criticality associated to each defect. This fundamental information for the design of components can be obtained only through fatigue tests or through an approach that combines micro-CT inspections and the local stress close to the defect provided by FEAs, allowing to assess the probability of failure associated with a specific defect [52] or its SIF. However, it must be also noted that micro-CT scans do not provide

information on local material weaknesses or interactions between small and adjacent defects that could significantly affect the fatigue response.

Let us focus now on the thermographic results from the fatigue cycling at increasing stress amplitude. The analysis of the thermal images (or thermograms) allows for estimating different thermal quantities, characteristic of the loading stress amplitude. Typically, all the collected thermomechanical quantities experience two regimes, identifying the breakup stress. This corresponds to the thermographic estimation of the fatigue strength, which can be defined as the limit stress to detect high self-heating due to the progressive and irreversible fatigue damage occurring in the material. According to the literature, this technique is rapid [15,26,53,54] because it allows identifying the fatigue strength with a very limited number of specimens and number of cycles.

Indeed, from the results of the thermally monitored fatigue tests given in Figure 8, it is immediate to state that all the tested specimens provide univocal feedback in terms of mechanical and thermal trends, allowing for good repeatability within the same batch, e.g. evidencing the robustness of the method. Indeed, the difference between the two thermal treatments is evident; the specimens thermally treated at 244°C have higher performances than those at 320°C. All plots in Figure 8 experience an initial linear trend that is flat or with a very low slope (primary regime) at low stress amplitudes. Then, it is followed by a progressive increase as a function of the applied stress. Here, the analysed quantities, e.g., the four thermal (dT/dN, ΔT_{stab}, Q and *D-mode*) and the two mechanical (W and $\Delta\varepsilon_p$) ones, are not bi-linear as a function of σ_a. Indeed, it is clear that the second part of the curve has an exponential or polynomial trend (secondary regime), evidencing the increase in fatigue damage.

Before moving to the estimated thermographic fatigue strength, some observations can be qualitatively drawn from the trends of these thermal quantities as a function of σ_a. First of all, it is possible to observe that data resulting from the ΔT_{stab} and the *D-mode* (Figure 8b,c) show higher scatter than the other plots of Figure 8; this scatter is related to the very small values measured especially during the first cycling blocks. Despite this scatter, ΔT_{stab} and *D-mode* also allow identifying the stress corresponding to the change in their thermographic behaviour.

Besides, it is worth noting that Q and W trends are very similar (Figure 8d,e). Their ratio is $Q \approx 50\text{-}55\% W$ for both the series, i.e., this is the percentage of mechanical work transformed into self-heating of the specimen. Indeed, W and Q are dual parameters. The mechanical work W is not a linear function of the applied stress, because of mechanical dissipation due to irreversible phenomena, such as plasticity, viscosity, inner friction and fatigue damages. This results

in the change of the hysteresis loops given in Figure 3e, as well as of $\Delta\varepsilon_p$ trend in Figure 8f. This mechanical behaviour is also reflected in Q, which summarizes the dissipative heat from the irreversible sources.

Literature suggested different methods to interpolate all these collected thermal quantities as a function of the applied stress and to estimate the thermographic fatigue strength, e.g. with one [15] or two straight lines [55,56], by an iterative approach [57], and by checking the determination coefficient of the fitting to identify the change in the curvature [54]. A recent work by Douellou et al [53] applied the thermographic technique to determine the fatigue strength of maraging AM specimens, interpolating the thermal data as a function of the applied stress with an exponential or spline fitting for the secondary regime, checking both the variation in the second and first derivatives. According to Yang et al [58], who also focused on the fatigue performance of additively manufactured AlSi10Mg specimens, the primary regime is dominated by internal friction related to the micro-displacement of the material microstructure and the intensity of the stress, while the secondary regime is dominated by the dissipation related to fatigue damage, such as micro-crack propagation. The transition between these two regimes, i.e., the thermographic fatigue strength, is difficult to estimate and a criterion is necessary. The early-stage automated method proposed by De Finis et al [32,59] is selected to identify univocally a threshold in the thermal behaviour and the corresponding thermographic fatigue strength. This method is a very suitable approach for the analysis of our thermal data, because of the polynomial trend of the secondary regime.

The fatigue strength estimated with the different proposed quantities is very similar for each specimen and among the specimens of each series (see Table 3). This is reflected in the low scatter bands of Figure 9; for this reason, an average from all these values for each series is calculated, independently of the specimens or the quantities used for the fatigue strength estimation. The average values of the fatigue strength are 118±11 MPa and 91±7 MPa, for HT-244 and HT-320 respectively, without intersection between the two series. Hence, these fatigue results underline statistically the different effect of the thermal treatment on the same additive material, with a greatly positive effect of the first thermal treatment on the fatigue performance, as previously evidenced in a study on horizontally additive manufactured specimens, made with the same material [41].

One of the open issues in the interpretation of these self-heating data regards the type of damage/damages detected by IR thermography, as well as the number of cycles corresponding to the thermographic fatigue strength. In the case of AM specimens or components, the dissipative phenomena detected with a thermal camera can be related to pre-existing defects generated during the manufacturing, and to the damage cumulated during fatigue loading. Therefore, to better understand the thermal measurements during fatigue cycling, averaged over the monitored area, it is

important to map the existing defects with the tomography, as well as to eventually relate these measurements with the fatigue life at high and very high cycles. Indeed, most of the literature works related the thermographic fatigue strength with the fatigue limit obtained from the classical Stair-Case method typically estimated between $2 \cdot 10^6$ and 10^7 cycles, e.g. [26,57,60], and with the fatigue strength estimation from numerical methods [61,62]. Instead, others also evidenced that the thermographic fatigue strength can be lower than the fatigue limit estimated by these methodologies, as in the case of aluminium alloys [32].

Hence, it is possible to compare now the thermographic fatigue strength with the P-S-N curves estimated from ultrasonic fatigue tests (Figure 11). Essentially, they show an overlap of the VHCF response for both heat-treated specimens. However, the two heat-treatments exhibit significantly different slopes in the S-N curves, which may be responsible for different fatigue strengths in the HCF regime, in agreement with the results of the thermographic methods. This is also confirmed by Figure 15, where, for both specimen types, the cdf of the fatigue life (with the abscissa axis in a logarithmic scale) is plotted for a stress value equal to the median fatigue strength estimated with the thermographic methods.

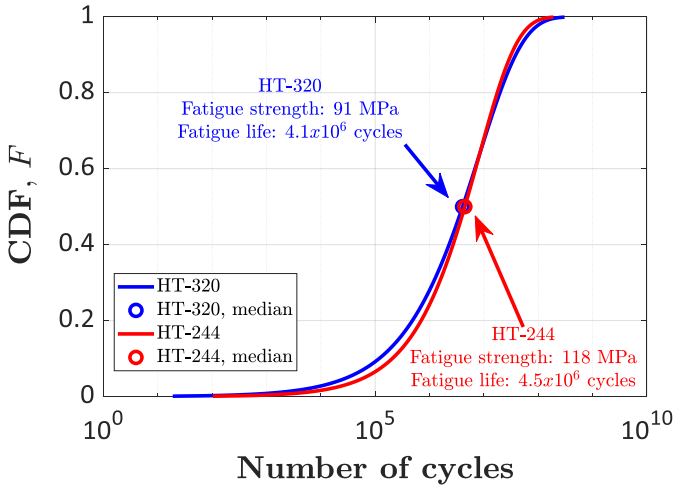

Figure 15: Cumulative distribution functions of the fatigue life at an applied stress equal to the fatigue strength estimated with the thermography.

As shown in Figure 15, when the applied stress equals the median fatigue strength estimated with the thermography, then the median fatigue life falls in the HCF range (4.1×10^6 cycles for HT-320 and 4.5×10^6 cycles for HT-244). Thus, it is possible to confirm that the thermographic method estimates the fatigue strength in the HCF regime [26,57,60]. This could be the reason for the better performance of the HT-244 specimen with respect to the HT-320 specimen when the fatigue strength is estimated with the thermography.

To conclude this discussion, Table 5 compares the implemented techniques on the AlSi10Mg specimen and summarizes the comments here proposed. In particular, it is clear that the testing time supports the use of these techniques as rapid tools for fatigue life estimation. This information can be useful to select the most suitable technique to estimate the fatigue strength also on other AM materials.

Table 5: Strength and weaknesses of the investigated techniques for the estimation of the fatigue strength of AM components.

Technique	Duration	Strengths	Weaknesses
Micro-CT inspections	About 4 hours a specimen + post-processing time	– Complete overview on the defect population – Detailed information on defects' location and morphology – 3D image of defects – Ideal for quality control of manufactured components	– Does not provide information on the criticality of defects – Resolution as high as possible to assess the criticality of interacting non-critical defects – No information on local material weakness
Fatigue tests with thermographic monitoring	Max 3 hours a specimen + post-processing time	– Theoretically, the fatigue strength can be estimated from only one specimen – Robust estimations – Can detect the effect of different thermal treatments on the fatigue strength, reflecting changes in microstructure and hardness	- Cannot evidence the single defect - Cannot measure the number of cycles associated to the fatigue strength
Ultrasonic fatigue tests with fractographic analysis	About 4 days for a complete characterization of one material	– HCF and VHCF characterization – Estimation of P-S-N curves – Estimation of statistical distribution of killer defects	- Test duration is not limited - Test duration is affected by internal damping of material and consequent self-heating of the specimen - Characterization may be affected by strain-rate effects

Table 6 reports the fatigue strengths estimated with the three investigated methodologies, i.e., the fatigue strength obtained starting from the analysis of the defect population with micro-CT inspections and the application of the El Haddad model, the fatigue strength assessed with the thermographic technique and the median fatigue strength at $4 \cdot 10^6$ cycles estimated by considering the ultrasonic fatigue test results and the step test procedure. Experimental data are obtained through tests carried out at different frequencies. In particular, the loading frequency in ultrasonic fatigue tests is significantly larger than that of conventional tests and its influence is still a debated subject in the literature. In

[63], experimental tests have been carried out on traditionally built specimens made of Aluminium alloys. The experimental results showed that an influence of the testing frequency can be excluded for these types of alloys. However, this is not a general rule, but an influence of the loading frequency can be mainly observable, even for Aluminium alloys, at large applied strain amplitudes close to the yield stress. However, ultrasonic fatigue tests in the present paper have been carried out at small stress amplitude in the elastic range, significantly below the yield stress. Moreover, in [64] experimental tests on AlSi10Mg alloy specimens produced through an SLM process and with properties similar to those of the specimens tested in the present paper have been carried out at 20 Hz and at 20 kHz. The experimental results proved that the loading frequency does not influence the fatigue response, with the data collected at 20 Hz close to the data obtained through tests at 20 kHz, with the limited difference mainly ascribed to the experimental scatter. Accordingly, an influence of the loading frequency can be excluded for the tested AlSi10Mg alloy and the experimental data obtained with the investigated techniques can be reliably compared.

Table 6: Comparison of the fatigue strength estimated with the investigated techniques (for the ultrasonic fatigue tests, the median fatigue strength close to $4 \cdot 10^6$ cycles is reported).

Specimen condition	Micro-CT	IR thermography	Ultrasonic fatigue testing
HT-244	[107-125] MPa	118±11 MPa	118 MPa (at $4 \cdot 10^6$cycles)
HT-320	[89-101] MPa	91±7 MPa	91 MPa (at $4 \cdot 10^6$cycles)

According to Table 6, the estimated fatigue strengths are close to each other, with limited differences. Table 6 confirms that the three investigated techniques can be reliably employed for the design of AM components, with strengths and weaknesses discussed in this Section. As highlighted previously, the fatigue strength estimated starting from the micro-CT analysis is based on assumed material parameters that can be reliably retrieved from available literature models for traditionally built materials. This represents an appropriate strategy if the required data required for the application of the El Haddad model are not available. However, since the AM part properties are strongly affected by the manufacturing process parameters, experimental tests for the assessment of the required material parameters are suggested, to provide more reliable results.

5. Conclusions

The paper compared and investigated three methodologies for the assessment of the fatigue response of AlSi10Mg specimens produced through an SLM process. Experimental tests have been carried out on specimens produced with the Selective Laser Melting (SLM) technique and subjected to two heat treatments characterized by a heating temperature of 320°C (HT-320) and a heating temperature of 244°C (HT-244).

The following general conclusions, which can be extended also to other materials produced with AM techniques, can be drawn:

1) Micro-CT scans provide detailed information on the defect population, which is of fundamental importance for AM components whose response is controlled by manufacturing defects. The analyses in the paper further confirm that the most critical defects, i.e., the one from which the fatigue crack originates and that must be considered when components are to be designed, may not be the largest within the loaded volume. Accordingly, the critical defect size to be considered for the design of components with literature models (e.g., the El Haddad model) should be defined by exploiting the information on the defect size and location provided by micro-CT analyses and by comparing the Stress Intensity Factor (SIF) associated to each defect.
2) Fatigue tests at increasing stress amplitude experience progressive self-heating, which was monitored with an IR thermal camera. The trend of the thermographic quantities collected during these cycles as a function of the applied stress allowed estimating the thermographic fatigue strength with a limited number of specimens, and faster than other standard techniques, e.g., the Staircase method.
3) Ultrasonic fatigue tests allow to rapidly assess the fatigue response of the investigated AlSi10Mg specimen. A "step-stress test" scheme has been followed and the experimental data have been analysed with a statistical method that models the damage accumulation during each loading step. To actually validate the rapid testing procedure, the HT-244 specimens have been tested to accelerate as much as possible the VHCF characterization. If the HT-244 dataset is considered, the maximum number of steps is equal to three and the total testing time is smaller than four days. The ultrasonic fatigue tests thus permit to complete the VHCF characterization of a new AM material and to get relevant information about its defect population in less than a week.

   By taking into account the investigated aluminium alloy, the estimated P-S-N curves have shown an essential overlap of the VHCF response of both specimen types. However, the different slopes of the estimated P-S-N

curves may be responsible of the better performance of HT-244 specimens in the HCF regime, also confirmed by the thermographic methods.

To conclude, the thermography technique and ultrasonic fatigue tests proved to be effective for a rapid estimation of the fatigue response of AM parts. Moreover, the analysis of the fracture surface permits also to assess the distribution of the critical defect sizes. On the other hand, also the results of micro-CT scans of specimens proved reliable in assessing the fatigue strength that can be employed for the design of parts. The use of this technique is suggested for the inspection of large volumes typical of components, where the largest defect (i.e., size effect) can be identified within the defects population. Indees, the other investigated techinques and the traditional tests would not allow for this identification. Depending on the safety requirement, the information on the entire population of defects from the micro-CT inspection in the component can be reliably exploited for its redesign or for quality control. However, the assessment of the limit stress starting from the defect population assessed on small volume specimens with literature models may require material parameters that can be estimated only with time-consuming experimental tests. Besides, this technique does not provide information on local material weaknesses or high residual stresses, which can be reliably assessed with the other investigated methodologies.

References

[1] Blakey-Milner B, Gradl P, Snedden G, Brooks M, Pitot J, Lopez E, et al. Metal additive manufacturing in aerospace: A review. Mater Des 2021;209. https://doi.org/10.1016/j.matdes.2021.110008.

[2] Martin JH, Yahata BD, Hundley JM, Mayer JA, Schaedler TA, Pollock TM. 3D printing of high-strength aluminium alloys. Nature 2017;549:365–9. https://doi.org/10.1038/nature23894.

[3] Olakanmi EO, Cochrane RF, Dalgarno KW. A review on selective laser sintering/melting (SLS/SLM) of aluminium alloy powders: Processing, microstructure, and properties. Prog Mater Sci 2015;74:401–77. https://doi.org/10.1016/j.pmatsci.2015.03.002.

[4] Yan Q, Song B, Shi Y. Comparative study of performance comparison of AlSi10Mg alloy prepared by selective laser melting and casting. J Mater Sci Technol 2020;41:199–208. https://doi.org/10.1016/j.jmst.2019.08.049.

[5] Fiocchi J, Tuissi A, Biffi CA. Heat treatment of aluminium alloys produced by laser powder bed fusion: A review. Mater Des 2021;204. https://doi.org/10.1016/j.matdes.2021.109651.

[6] CEN European Committee for Standardization. Eurocode 3 - Design of steel structures - Part 1-9: Fatigue 2005.

[7] CEN European Committee for Standardization. Eurocode 9 - Design of aluminium structures - Part 1-3: Structures susceptible to fatigue 2021.

[8] Pyttel B, Schwerdt D, Berger C. Very high cycle fatigue - Is there a fatigue limit? Int J Fatigue 2011;33:49–58. https://doi.org/10.1016/j.ijfatigue.2010.05.009.

[9] Biffi CA, Bassani P, Fiocchi J, Albu M, Tuissi A. Selective laser melting of AlCu-TiB2 alloy using pulsed wave laser emission mode: processability, microstructure and mechanical properties. Mater Des 2021;204. https://doi.org/10.1016/j.matdes.2021.109628.

[10] Fu J, Li H, Song X, Fu MW. Multi-scale defects in powder-based additively manufactured metals and alloys. J Mater Sci Technol 2022;122:165–99. https://doi.org/10.1016/j.jmst.2022.02.015.

[11] Mughrabi H. Specific features and mechanisms of fatigue in the ultrahigh-cycle regime. Int J Fatigue 2006;28:1501–8. https://doi.org/10.1016/j.ijfatigue.2005.05.018.

[12] Romano S, Brückner-Foit A, Brandão A, Gumpinger J, Ghidini T, Beretta S. Fatigue properties of AlSi10Mg obtained by additive manufacturing: Defect-based modelling and prediction of fatigue strength. Eng Fract Mech 2018;187:165–89. https://doi.org/10.1016/j.engfracmech.2017.11.002.

[13] Leuders S, Thöne M, Riemer A, Niendorf T, Tröster T, Richard HA, et al. On the mechanical behaviour of titanium alloy TiAl6V4 manufactured by selective laser melting: Fatigue resistance and crack growth performance. Int J Fatigue 2013;48:300–7. https://doi.org/10.1016/j.ijfatigue.2012.11.011.

[14] Romano S, Abel A, Gumpinger J, Brandão AD, Beretta S. Quality control of AlSi10Mg produced by SLM : Metallography versus CT scans for critical defect size assessment. Addit Manuf 2019;28:394–405. https://doi.org/10.1016/j.addma.2019.05.017.

[15] La Rosa G, Risitano A. Thermographic methodology for rapid determination of the fatigue limit of materials and mechanical components. Int J Fatigue 2000;22:65–73. https://doi.org/10.1016/S0142-1123(99)00088-2.

[16] Stanzl-Tschegg S. Very high cycle fatigue measuring techniques. Int J Fatigue 2014;60:2–17. https://doi.org/10.1016/j.ijfatigue.2012.11.016.

[17] Fiocchi J, Tuissi A, Bassani P, Biffi CA. Low temperature annealing dedicated to AlSi10Mg selective laser melting products. J Alloys Compd 2017;695:3402–9. https://doi.org/10.1016/j.jallcom.2016.12.019.

[18] Fiocchi J, Biffi CA, Colombo C, Vergani LM, Tuissi A. Ad Hoc Heat Treatments for Selective Laser Melted AlSi10Mg Alloy Aimed at Stress-Relieving and Enhancing Mechanical Performances. JOM 2020;72. https://doi.org/10.1007/s11837-019-03973-z.

[19] Paolino DS, Tridello A, Chiandussi G, Rossetto M. On specimen design for size effect evaluation in ultrasonic gigacycle fatigue testing. Fatigue Fract Eng Mater Struct 2014;37:570–9. https://doi.org/10.1111/ffe.12149.

[20] Tridello A. VHCF response of Gaussian specimens made of high-strength steels: comparison between unrefined and refined AISI H13. Fatigue Fract Eng Mater Struct 2017;40:1676–89. https://doi.org/10.1111/ffe.12610.

[21] Murakami Y. Metal Fatigue: Effects of Small Defects and Nonmetallic Inclusions. Elsevier Ltd; 2002.

[22] du Plessis A, Yadroitsava I, Yadroitsev I. Effects of defects on mechanical properties in metal additive manufacturing: A review focusing on X-ray tomography insights. Mater Des 2020;187:108385. https://doi.org/10.1016/j.matdes.2019.108385.

[23] Meneghetti G, Ricotta M. Estimating the intrinsic dissipation using the second harmonic of the temperature signal in tension-compression fatigue: Part I. Theory. Fatigue Fract Eng Mater Struct 2021;44:2168–85. https://doi.org/10.1111/ffe.13485.

[24] Guo Q, Guo X, Fan J, Syed R, Wu C. An energy method for rapid evaluation of high-cycle fatigue parameters based on intrinsic dissipation. Int J Fatigue 2015;80:136–44. https://doi.org/10.1016/j.ijfatigue.2015.04.016.

[25] Brémond P. New developments in Thermo Elastic Stress Analysis by Infrared Thermography. IV Conf. Panam. END, Buenos Aires: 2007.

[26] Colombo C, Sansone M, Patriarca L, Vergani L. Rapid estimation of fatigue limit for C45 steel by thermography and digital image correlation. J Strain Anal Eng Des 2021;56:478–91. https://doi.org/10.1177/0309324720975284.

[27] Paynter RJH, Dutton AG. The use of a second harmonic correlation to detect damage in composite structures using thermoelastic stress measurements. Strain 2003;39:73–8. https://doi.org/10.1046/j.1475-1305.2003.00056.x.

[28] Vergani L, Colombo C, Libonati F. A review of thermographic techniques for damage investigation in composites. Frat Ed Integrita Strutt 2014;8:1–12. https://doi.org/10.3221/IGF-ESIS.27.01.

[29] Meneghetti G, Ricotta M. The heat energy dissipated in the material structural volume to correlate the fatigue crack growth rate in stainless steel specimens. Int J Fatigue 2018;115:107–19. https://doi.org/10.1016/j.ijfatigue.2018.07.037.

[30] Meneghetti G. Analysis of the fatigue strength of a stainless steel based on the energy dissipation. Int J Fatigue 2007;29:81–94. https://doi.org/10.1016/j.ijfatigue.2006.02.043.

[31] Rousselier G. Dissipation in porous metal plasticity and ductile fracture. J Mech Phys Solids 2001;49:1727–46. https://doi.org/10.1016/S0022-5096(01)00013-8.

[32] De Finis R, Palumbo D, Ancona F, Galietti U. Fatigue limit evaluation of various martensitic stainless steels with new robust thermographic data analysis. Int J Fatigue 2015;74:88–96. https://doi.org/10.1016/j.ijfatigue.2014.12.010.

[33] Lee Y, Makam S, Mckelvey S, Lu M. Durability Reliability Demonstration Test Methods. Procedia Eng 2015;133:31–59. https://doi.org/10.1016/j.proeng.2015.12.621.

[34] Nelson WB. Accelerated Testing: Statistical Models, Test Plans, and Data Analysis. Wiley; 1990.

[35] Benard A, Bos-Levenbach EC. The plotting of observations on probability paper. Stat Neerl 1953;7:163–73.

[36] Wu Z, Wu S, Bao J, Qian W, Karabal S, Sun W, et al. The effect of defect population on the anisotropic fatigue resistance of AlSi10Mg alloy fabricated by laser powder bed fusion. Int J Fatigue 2021;151:106317. https://doi.org/10.1016/j.ijfatigue.2021.106317.

[37] Masuo H, Tanaka Y, Morokoshi S, Yagura H, Uchida T, Yamamoto Y, et al. Influence of defects, surface roughness and HIP on the fatigue strength of Ti-6Al-4V manufactured by additive manufacturing. Int J Fatigue 2018;117:163–79. https://doi.org/10.1016/j.ijfatigue.2018.07.020.

[38] Rigon D, Meneghetti G. An engineering estimation of fatigue thresholds from a microstructural size and Vickers hardness: application to wrought and additively manufactured metals. Int J Fatigue 2020;139:105796. https://doi.org/10.1016/j.ijfatigue.2020.105796.

[39] Beretta S, Romano S. A comparison of fatigue strength sensitivity to defects for materials manufactured by AM or traditional processes. Int J Fatigue 2017;94:178–91. https://doi.org/10.1016/j.ijfatigue.2016.06.020.

[40] Stanzl-Tschegg SE, Mayer HR, Beste A, Kroll S. Fatigue and fatigue crack propagation in AlSi7Mg cast alloys under in-service loading conditions. Int J Fatigue 1995;17:149–55. https://doi.org/10.1016/0142-1123(95)95895-N.

[41] Tridello A, Fiocchi J, Biffi CA, Chiandussi G, Rossetto M, Tuissi A, et al. Effect of microstructure, residual stresses and building orientation on the fatigue response up to 109 cycles of an SLM AlSi10Mg alloy. Int J Fatigue 2020;137. https://doi.org/10.1016/j.ijfatigue.2020.105659.

[42] Maskery I, Aboulkhair NT, Corfield MR, Tuck C, Clare AT, Leach RK, et al. Quantification and characterisation of porosity in selectively laser melted Al-Si10-Mg using X-ray computed tomography. Mater Charact 2016;111:193–204. https://doi.org/10.1016/j.matchar.2015.12.001.

[43] Yang K V., Rometsch P, Davies CHJ, Huang A, Wu X. Effect of heat treatment on the microstructure and anisotropy in mechanical properties of A357 alloy produced by selective laser melting. Mater Des 2018;154:275–90. https://doi.org/10.1016/j.matdes.2018.05.026.

[44] Le VD, Pessard E, Morel F, Edy F. Interpretation of the fatigue anisotropy of additively manufactured TA6V alloys via a fracture mechanics approach. Eng Fract Mech 2019;214:410–26. https://doi.org/10.1016/j.engfracmech.2019.03.048.

[45] Colombo C, Biffi CA, Fiocchi J, Scaccabarozzi D, Saggin B, Tuissi A, et al. Modulating the damping capacity of SLMed AlSi10Mg trough stress-relieving thermal treatments. Theor Appl Fract Mech 2020;107:1–6. https://doi.org/10.1016/j.tafmec.2020.102537.

[46] Bagherifard S, Beretta N, Monti S, Riccio M, Bandini M, Guagliano M. On the fatigue strength enhancement of additive manufactured AlSi10Mg parts by mechanical and thermal post-processing. Mater Des 2018;145:28–41. https://doi.org/10.1016/j.matdes.2018.02.055.

[47] Beretta S, Gargourimotlagh M, Foletti S, du Plessis A, Riccio M. Fatigue strength assessment of “as built”

AlSi10Mg manufactured by SLM with different build orientations. Int J Fatigue 2020;139:105737. https://doi.org/10.1016/j.ijfatigue.2020.105737.

[48] Salmi A, Atzeni E. History of residual stresses during the production phases of AlSi10Mg parts processed by powder bed additive manufacturing technology. Virtual Phys Prototyp 2017;12:153–60. https://doi.org/10.1080/17452759.2017.1310439.

[49] Maamoun AH, Elbestawi MA, Veldhuis SC. Influence of shot peening on alsi10mg parts fabricated by additive manufacturing. J Manuf Mater Process 2018;2. https://doi.org/10.3390/jmmp2030040.

[50] Tammas-Williams, S, Withers PJ, Todd I, Prangnell PB. The Influence of Porosity on Fatigue Crack Initiation in Additively Manufactured Titanium Components. Sci Rep 2017;7:1–13. https://doi.org/10.1038/s41598-017-06504-5.

[51] Akgun E, Zhang X, Lowe T, Zhang Y, Dor M. Fatigue of laser powder-bed fusion additive manufactured Ti-6Al-4V in presence of process-induced porosity defects 2022;259. https://doi.org/10.1016/j.engfracmech.2021.108140.

[52] Romano S, Miccoli S, Beretta S. A new FE post-processor for probabilistic fatigue assessment in the presence of defects and its application to AM parts. Int J Fatigue 2019;125:324–41. https://doi.org/10.1016/j.ijfatigue.2019.04.008.

[53] Douellou C, Balandraud X, Duc E, Verquin B, Lefebvre F, Sar F. Rapid characterization of the fatigue limit of additive-manufactured maraging steels using infrared measurements. Addit Manuf 2020;35. https://doi.org/10.1016/j.addma.2020.101310.

[54] Huang J, Pastor ML, Garnier C, Gong X. Rapid evaluation of fatigue limit on thermographic data analysis. Int J Fatigue 2017;104:293–301. https://doi.org/10.1016/j.ijfatigue.2017.07.029.

[55] Luong MP. Fatigue limit evaluation of metals using an infrared thermographic technique. Mech Mater 1998;28:155–63. https://doi.org/10.1016/S0167-6636(97)00047-1.

[56] Colombo C, Libonati F, Vergani L. Fatigue damage in GFRP. Int J Struct Integr 2012;3:424–40. https://doi.org/10.1108/17579861211281218.

[57] Curà F, Curti G, Sesana R. A new iteration method for the thermographic determination of fatigue limit in steels. Int J Fatigue 2005;27:453–9. https://doi.org/10.1016/j.ijfatigue.2003.12.009.

[58] Yang C, Zhu K, Liu Y, Cai Y, Liu W, Zhang K, et al. A comparative study of fatigue energy dissipation of additive manufactured and cast Alsi10Mg alloy. Metals (Basel) 2021;11. https://doi.org/10.3390/met11081274.

[59] De Finis R, Palumbo D, Serio LM, De Filippis LAC, Galietti U. Correlation between thermal behaviour of AA5754-H111 during fatigue loading and fatigue strength at fixed number of cycles. Materials (Basel) 2018;11. https://doi.org/10.3390/ma11050719.

[60] Li XD, Zhang H, Wu DL, Liu X, Liu JY. Adopting lock-in infrared thermography technique for rapid determination of fatigue limit of aluminum alloy riveted component and affection to determined result caused by initial stress. Int J Fatigue 2012;36:18–23. https://doi.org/10.1016/j.ijfatigue.2011.09.005.

[61] Mehdizadeh M, Haghshenas A, Khonsari MM. In-situ Technique for Fatigue Life Prediction of Metals Based on Temperature Evolution. Int J Mech Sci 2021;192. https://doi.org/10.1016/j.ijmecsci.2020.106113.

[62] Colombo C, Bhujangrao T, Libonati F, Vergani L. Effect of delamination on the fatigue life of GFRP: A thermographic and numerical study. Compos Struct 2019;218:152–61. https://doi.org/10.1016/j.compstruct.2019.03.023.

[63] Stanzl-Tschegg SE, Mayer H. Fatigue and fatigue crack growth of aluminium alloys at very high numbers of cycles. Int J Fatigue 2001;23:231–7. https://doi.org/10.1016/s0142-1123(01)00167-0.

[64] Awd M, Siddique S, Johannsen J, Emmelmann C, Walther F. Very high-cycle fatigue properties and microstructural damage mechanisms of selective laser melted AlSi10Mg alloy. Int J Fatigue 2019;124:55–69. https://doi.org/10.1016/j.ijfatigue.2019.02.040.